scientific reports

Check for updates

OPEN

Magnetism and hidden quantum geometry in charge neutral twisted trilayer graphene

Alina Wania Rodrigues[1]✉, Maciej Bieniek[2], Daniel Miravet[1] & Paweł Hawrylak[1]

Here we present a theory of mirror-symmetric magic angle twisted trilayer graphene. The electronic properties are described by a Hubbard model with long range tunneling matrix elements. The electronic properties are obtained by solving the mean field Hubbard model. We obtain the bandstructure with characteristic flat bands and a Dirac cone. At charge neutrality, turning on electron-electron interactions results in metallic to antiferromagnetic phase transition, for Hubbard interaction strength considerably smaller than in other graphene multilayers. We analyze the stability of the antiferromagnetic state against the symmetry breaking induced by hexagonal boron nitride encapsulation, and mirror symmetry breaking caused by the application of electric fields that mix the Dirac cone with the flat bands. Additionally, we explore the topological properties of the system, revealing a hidden quantum geometry. Despite the flat bands having zero Chern numbers, the multiband Berry curvature distribution over the moiré Brillouin zone exhibits a non-trivial structure. Finally, we propose a mechanism to tune this quantum geometry, providing a pathway to control the system's topological properties.

Moiré materials offer a promising platform for designing tunable simulators of strongly correlated systems. The mismatch of the lattice constants or misalignment of the atomically-thin stacked layers leads to superlattice periodicity, which, for specific twist angles, flattens the bands around the Fermi energy. The flat bands enhance the role of the electron-electron interactions, leading to the observation of insulating and superconducting phases[1,2] for bilayer graphene twisted by the so-called magic angle[3]. Following this discovery, a significant number of moiré systems has been realized with different number of layers and sequences of twist angles, including, but not limited to, mirror-symmetric trilayers[4–6], helical trilayers[7], double bilayers[8] and pentalayers[9]. Some of these have been shown to host a number of correlated and topological states such as correlated insulators[1,10–15], quantum anomalous Hall effect[16], ferromagnetism[17] and a generalized Wigner crystal state[18].

Mirror-symmetric magic angle twisted trilayer graphene (TTG) consists of a middle layer rotated by the magic angle relative to two aligned top and bottom layers[19]. The band structure of TTG features two flat bands (per spin and valley) near the Fermi level, alongside Dirac cones that intersect the gap at the K points[19–27]. These features are also observed in ARPES experiments[28]. The spectrum of TTG is highly tunable through several external parameters, including the electric field, the hexagonal boron nitride (hBN) alignment, and the twist angle. Compared to twisted bilayer graphene (TBG), TTG offers a highly stable and versatile platform for engineering electronic states. Notably, TTG demonstrates robust and reproducible superconductivity across a wide range of tuning parameters[4,5,629–44]. Consequently, TTG has been the focus of an extensive theoretical investigation, employing both continuum models[19,21–24,27] and atomistic approaches, such as *ab initio*[20,45] and tight-binding[45]. Interaction effects in TTG have been explored in Refs.[23,26,46], while theoretical descriptions of its superconducting phase are proposed in Refs.[45,47–49]. Additionally, the phonon properties of TTG were studied in Ref.[50]. Despite these significant advances, a unified theory of TTG is still lacking. Many of its properties, including the magnetic and topological phase diagrams, remain elusive.

In this work, we consider the atomistic tight-binding Hamiltonian combined with a Hubbard interaction term and apply the self-consistent collinear Hartree-Fock method to determine the magnetic properties of the ground state. Our primary focus is on the transition from the paramagnetic to the antiferromagnetic (AF) phase, a phenomenon extensively studied in monolayer graphene systems[51–53]. It has been shown that the area in the parameter space of the AF phase increases as we increase the number of layers[54]. We analyze the magnetic phase diagrams as functions of interaction strength, mirror, and sublattice symmetry-breaking perturbations, which arise from applied electric fields and hBN encapsulation. Interestingly, the interplay between magnetic ordering

[1]Department of Physics, University of Ottawa, Ottawa, ON K1N 6N5, Canada. [2]Institute of Theoretical Physics, Wrocław University of Science and Technology, Wybrzeże Wyspiańskiego 27, 50-370 Wrocław, Poland. ✉email: awaniaro@uottawa.ca

and topological properties, such as the emergence of AF Chern insulators[55], offers a compelling framework to explore quantum geometry in these systems. We compute the quasiparticle multiband Chern numbers for the valence and conduction flat bands, revealing the distribution of multiband Berry curvature (mBC) across the moiré Brillouin zone (mBZ), and demonstrate its tunability in experimentally realistic scenarios. We refer to this phenomenon as hidden quantum geometry, since a vanishing Chern number would ordinarily indicate a topologically trivial system, whereas in this case a nontrivial distribution of Berry curvature persists. We note that in this study, we focus on the antisymmetric part of the quantum geometric tensor (known as Berry curvature), leaving the symmetric part (quantum metric) for future analysis[56]. We note also that the behavior of mBC in TTG differs from the TBG case, where the Γ point is the source of Berry's curvature[57]. In the trilayer instance, we can identify contributions both from the Γ and *K* points.

Results

Paramagnetic ground state, electric field- and hBN-induced gaps We begin with an analysis of the paramagnetic ground state of the system. The single-particle Hamiltonian is given by:

$$\hat{H}_{\mathrm{TB}} = \sum_{i,j}^{N} \sum_{\sigma} t(\vec{r}_i, \vec{r}_j)(c^{\dagger}_{i,\sigma} c_{j,\sigma} + c^{\dagger}_{j,\sigma} c_{i,\sigma}), \tag{1}$$

where hopping between p_z orbitals in three layers can be modeled as

$$\begin{aligned} t(\vec{r}_i, \vec{r}_j) =& (1-n^2)\gamma_0 \exp\left(\lambda_1\left(1 - \frac{|\vec{r}_i - \vec{r}_j|}{a}\right)\right) + \\ & n^2 \gamma_1 \exp\left(\lambda_2\left(1 - \frac{|\vec{r}_i - \vec{r}_j|}{c}\right)\right). \end{aligned} \tag{2}$$

Here *i*, *j* are the indices enumerating atoms. We note that terms γ_0 and γ_1 in Eq. (2) parametrize arbitrary distance hopping $t(r_i, r_j)$. In our calculations we consider up to the 6^{th} nearest neighbor, ensuring that effects such as trigonal warping and the electron-hole asymmetry are captured. We account for the electron-electron interactions through the Hubbard term:

$$\hat{H}_U = U \sum_i \hat{n}_{i\uparrow} \hat{n}_{i\downarrow}. \tag{3}$$

The parameters and further details are given in "Methods".

Figure 1a–c summarizes our system's geometry. The structure consists of top and bottom layers in AA stacking, with the middle layer twisted by an angle of $\theta = 1.55^{\circ}$. The TTG is encapsulated in aligned hBN, which is modeled as a staggered potential applied to the top and bottom layers: $\hat{H}_{\Delta_{\mathrm{hBN}}} = \Delta_{\mathrm{hBN}} \sum_{i,\sigma} \alpha_i |l_i| c^{\dagger}_{i,\sigma} c_{i,\sigma}$ where $l_i = 1, 0, -1$ for top, middle and bottom layers respectively and $\alpha_i = 1, -1$ when *i* belongs to sublattice A and B respectively. This way there is a $2\Delta_{\mathrm{hBN}}$ difference in onsite energy between A and B atoms of the top and bottom layers. Furthermore, a vertical electric field is introduced, modifying the potential difference between the top and bottom layers: $\hat{H}_{\Delta_V} = \frac{\Delta_V}{2} \sum_{i,\sigma} l_i c^{\dagger}_{i,\sigma} c_{i,\sigma}$. Therefore, the full Hamiltonian is given by

$$\hat{H} = \hat{H}_{\mathrm{TB}} + \hat{H}_{\mathrm{U}} + \hat{H}_{\Delta_{\mathrm{hBN}}} + \hat{H}_{\Delta_V}. \tag{4}$$

Since we assume a commensurate angle, i.e., periodic crystal structure, we can define a finite moiré unit cell (UC) (Fig. 1b) and mBZ (Fig. 1d). Each moiré UC consist of N_{at}, and each atom repeats in the UC creating N_{at} simple Bravais sublattices. We apply periodic boundary condition to obtain allowed wavevectors, associate a Bloch wavefunction for a given wavevector $\vec{k}$ with each atom in a moiré cell, and diagonalize resulting Hamiltonian matrix to obtain energy bands. Fig. 1e shows the result for the interaction strength $U = 0$. This procedure is described in greater detail in Ref.[58]. To find the low energy state of this Hamiltonian we use a self consistent collinear Hartree-Fock procedure, see details in "Methods". The resulting ground state is paramagnetic, meaning each atom has an equal spin population (with precision of 10^{-6}). We obtain the characteristic flat band at the Fermi level with two valence and two conduction bands for each spin component. In our calculation, we also reproduce the high velocity Dirac cones at moiré K points, with Dirac points approximately 15 meV below the Fermi level. We confirm that the wave functions of these Dirac cones are localized solely on the top and bottom layers, while the flat band's wave functions are localized 50% on the middle layer and 25% on the top and bottom (see Fig. 6 in SM). Such localization can be explained in terms of a TTG system comprising of a monolayer graphene and TBG[21].

We now study the effect of vertical electric field and hBN encapsulation. We first introduce a non-zero electric field ($\Delta_V = 120$ meV). Such mirror-symmetry breaking perturbation hybridizes the Dirac cones with the flat bands[23]. This hybridization leads to splitting between the valence and conduction bands in the flat band, opening a gap at *K* points, shown in Fig. 1f by a blue arrow. However, the gap at the Fermi level remains closed, and, in addition, the gap between the flat band and the remote bands closes at the Γ point.

In the next step, we turn on the interaction with encapsulating hBN in the form of a top and bottom layer staggered sublattice potential, see Fig. 1g ($\Delta_{\mathrm{hBN}} = 25$ meV). This leads to the opening of the gap within the

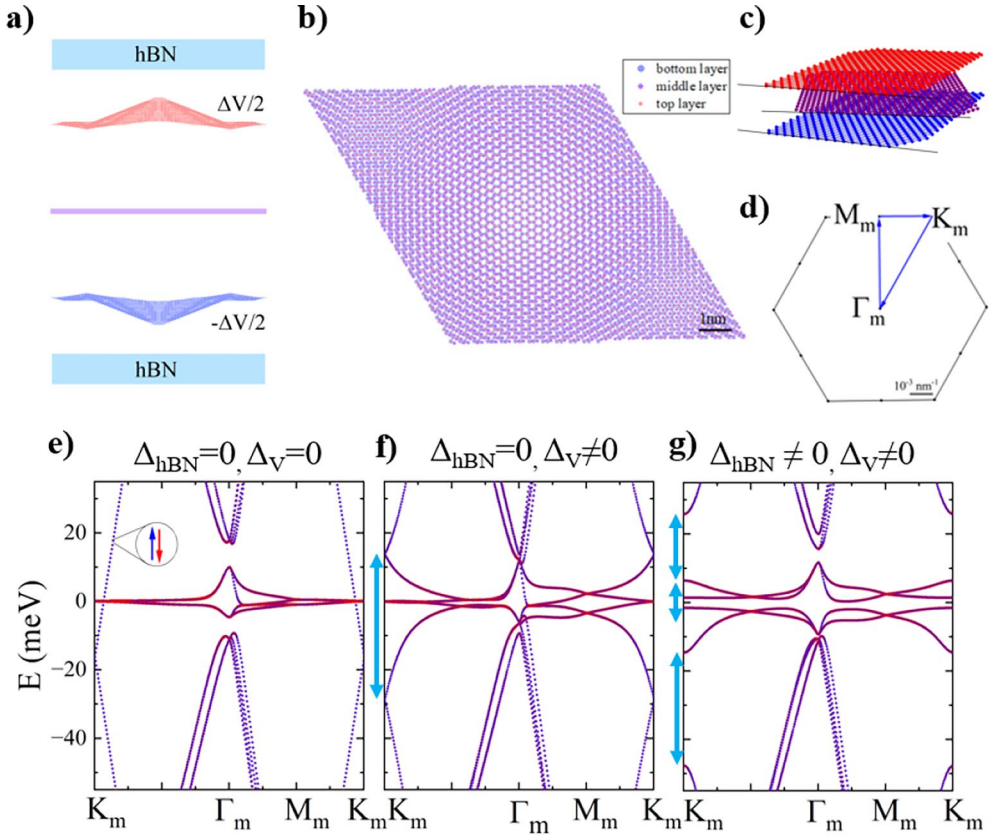

Fig. 1. Structural and electronic properties of TTG. (**a**) Side, (**b**) top, and (**c**) 3D view of geometry. TTG consists of three layers of graphene, with the middle one twisted by θ, with respect to the aligned top and bottom layers, which are relaxed out-of-plane. The system is encapsulated in aligned hBN, and a vertical electric field is applied. (**d**) mBZ with high symmetry points. (**e**) Band structure of pristine TTG. (**f**) Effect of non-zero electric field ($\Delta_V = 120$ meV) hybridizing Dirac cones with the flat band. (**g**) The combined effect of electric field and hBN encapsulation ($\Delta_V = 120$ meV, $\Delta_{\mathrm{hBN}} = 25$ meV), opening extra gaps near the Fermi level. The gaps opened by applying an electric field and hBN are marked with blue arrows.

flat band. Additionally, similar to the gapped monolayer graphene case[59], a gap between the Dirac cones opens and their dispersion becomes parabolic. The remote bands peel off from the flat band at the Γ point so that our system consists of a well defined flat band and a gap around the Fermi energy. We note that TTG with an applied electric field and hBN is, therefore, strikingly similar to the TBG/hBN structure, with an extra set of remote bands at *K* points originating from the gapped Dirac cones. These mechanisms lead to the redistribution of the wave function between the layers, however the main trends are preserved. More details of these mechanisms are available in SM.

Band gap and anti-ferromagnetic transition In the context of moiré materials, electron-electron interactions play an essential role due to the reduced bandwidth. To understand their influence, we consider different strengths of the interaction, modifying the Hubbard parameter *U*. We have tested several choices of initial input density and concluded that there is a phase transition between the non-magnetic and the AF state for the critical value of $U_c \approx 0.6t$, where $t = |\gamma_0| = 2.835$ eV is the nearest neighbor hopping. To determine the ground state of the system we analyze the total absolute magnetization (see "Methods"), which value is close to zero for a paramagnetic case, and significantly larger in the AF phase.

We now analyze the Hartree-Fock quasiparticle bands for spin up and down obtained by self-consistently diagonalizing Hubbard Hamiltonian, Eq. 4. For sufficiently small $U < U_c$, we do not observe any strong renormalization of the bands close to the Fermi level, as shown in Fig. 2a. The state is paramagnetic, meaning each atom has an equal spin population. On the other hand, when $U > U_c$, a transition to an AF ground state occurs. A clear band gap is opened in the flat band after the phase transition in Fig. 2b for $U > 1.1t$. There is no gap opening for the Dirac cones, therefore, no gap is generated at the Fermi level. The AF state has the most significant spin polarization in the middle layer, which is the layer with the highest contribution to the flat band. Bilayer graphene has smaller U_c than a monolayer, therefore the effect of *U* is stronger in the middle of TTG. The total spin density on A and B sublattices of graphene layers building TTG is imbalanced, producing a microscopic AF state. Such AF state is analogous to an AF state in other n-layer graphene systems[54,60]. We note that for the system to undergo a transition from a metallic to insulating state, the presence of an hBN substrate is necessary. Without it, the system is metallic both in the paramagnetic and antiferromagnetic states, while it remains insulating for all values of U and electric field with an hBN substrate present.

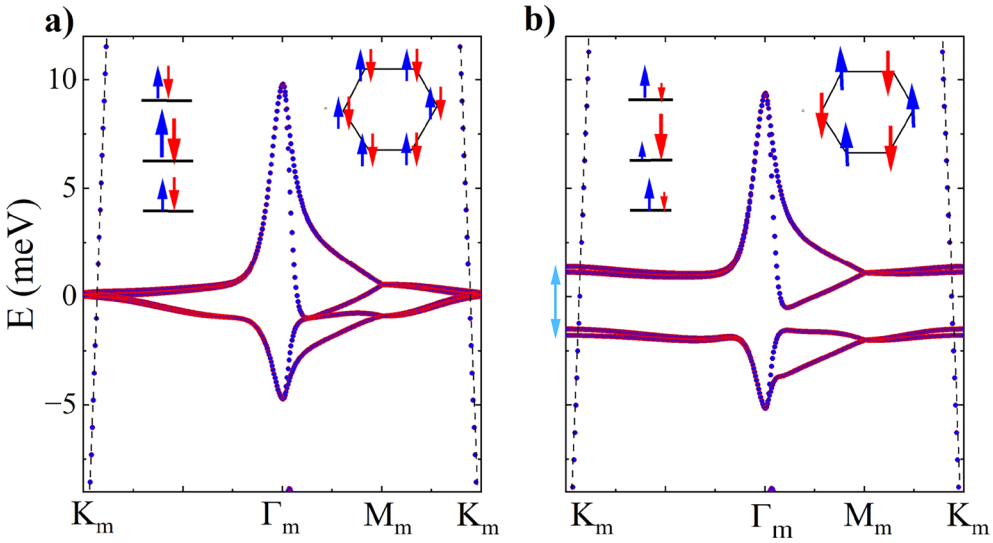

Fig. 2. Hartree-Fock quasiparticle band structures of TTG with $\Delta_V = \Delta_{\mathrm{hBN}} = 0$. (**a**) Band structure in the paramagnetic state with $U = 0.5t$. The insets show a schematic depiction of the spin configuration in the three layers (left) and on the honeycomb lattice of a single layer (right). Black dashed lines were added alongside the Dirac cone dispersion to improve readability. (**b**) Band structure of the flat band in the anti-ferromagnetic state with $U = 1.1t$. Red and blue colors encode up and down spins, respectively.

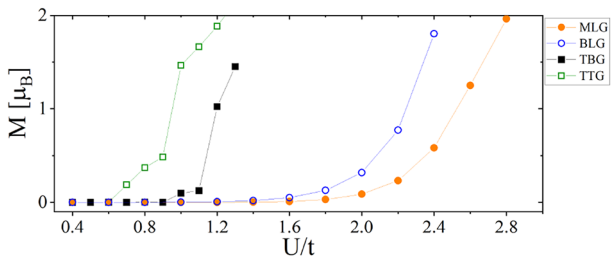

Fig. 3. AF transition in various graphene-based systems. Total absolute magnetization of different graphene systems (MLG, BLG, TBG, TTG) in the units of Bohr magneton as a function of the interaction U scaled by the nearest-neighbor hopping t.

The Hubbard parameter U for which the para- to anti-ferro- magnetic transition occurs is lower than in the mono- and bi-layer graphene systems (Fig. 3). For example, it has been shown that in the monolayer graphene (MLG) in the Hartree-Fock approximation $U_c \approx 2t$[54]. We reproduced this result in our model, with small differences caused by the long-range TB hopping necessary to model TTG correctly. Equivalent calculations for bilayer graphene (BLG) yield $U_c^{\mathrm{BLG}} < U_c^{\mathrm{MLG}}$. This stems from the fact that since the dispersion in BLG is parabolic, the density of states is increased, and the ratio of interactions to kinetic energy increases as well. It is not surprising then that TBG has a smaller critical transition parameter ($U = 1.1t$), as shown in Fig. 3. An extension of this Fig., showing the influence of the hBN substrate can be found in SM Fig. 7. It shows, that inclusion of the hBN can slower down the transition in both twisted bilayer and trilayer graphene, while it has negligible effect in untwisted systems. This is a consequence of the U_c/Δ_{hBN} ratio, which is larger in untwisted systems.

Naively, one could argue that since TTG has an additional Dirac cone and similar bandwidth of the flat bands, critical U should be larger than in TBG. Our results point out that there is actually an opposite trend with $U_c^{\mathrm{TTG}} < U_c^{\mathrm{TBG}}$. This effect is a consequence of the TTG flat band being flatter than the TBG one. Here, we refer to its pieces being effectively flatter since, at the Γ point, the flat band in TTG is actually wider (15 meV) than in TBG (8 meV). The flatter band enhances electron-electron interaction effects, reducing screening effects and further decreasing the critical Hubbard parameters.

We performed calculations for large U and concluded that the state with the lowest energy is still antiferromagnetic. Assuming ferromagnetic input (initial) state, we obtain energy difference between antiferromagnetic (ground) and ferromagnetic (higher in energy) states of 0.7193 meV. This value is consistent in order of magnitude with TBG system, see e.g. recent works of Hou et al.[61] and Sánchez Sánchez et al.[62], but at odds with Adhikari et al.[63] that claims obtaining ferromagnetic ground state at $\nu = 0$ for TBG.

We note also that, from an experimental perspective, the effective interaction strength can be tuned through several mechanisms, including dielectric engineering of the surrounding medium[64], adjusting the distance to metallic gates[65], varying the twist angle[66], or inducing strain[67]. In our modeling, however, both the twist angle and the atomic positions are kept fixed. Consequently, the only mechanism by which the interaction strength can vary in our setup is through changes in the dielectric environment (thickness of the hBN substrate) and distance to the metallic gates.

To experimentally verify our proposal of a paramagnetic to AFM ground state transition, standard techniques such as neutron scattering are likely impractical due to the monolayer nature of the system. Instead, more sensitive probes, such as spin-polarized scanning tunneling microscopy[68], magneto-optical spectroscopy[69] or magnetotransport[37,70,71] are necessary to establish the magnetic phase diagram of this system.

Magnetic phase diagram stability We now study the combined effects of the applied electric field, hBN encapsulation, and the presence of electron-electron interactions on the ground state of charge neutral TTG. We study the magnetic phase diagram as a function of the interaction strength and electric field for three values of the staggered potential from hBN encapsulation.

Our results are summarized in Fig. 4. Without the A/B sublattice symmetry breaking, we observe in Fig. 4a that the critical value of U increases with increasing electric field. This follows from the fact that the applied electric field breaks the mirror-symmetry of TTG and causes the system to bear more resemblance to three monolayers, for which the critical value of U/t is higher. Since in the actual device U/t is fixed, the electric field allows thus to switch magnetic state from AF to paramagnetic for sufficiently large U/t.

When small sublattice breaking perturbation is included in the top and bottom layers, even though most of the electron density is in the middle layer, a strong renormalization of the phase diagram is observed. The imbalance introduced by the hBN layer directly counteracts the effects of the Hubbard term. While the Hubbard interaction penalizes the occupation of different-spin electrons on the same atom, the hBN-induced potential favors relocating electrons to sublattice B. Consequently, a larger value of U is required to overcome this preference, transfer charge from sublattice B to sublattice A, and create a polarized state. The region of stable AF state is reduced to larger values of U/t and smaller electric field; see top left of Fig. 4b. Further increase of the staggered potential parameter, as in Fig. 4c to $\Delta_{\mathrm{hBN}} = 50$ meV, completely destroys AF region in the studied range of U/t. We confirm that the AF state is susceptible to mirror and sublattice symmetry-breaking perturbations.

Multiband Berry's curvature tuning Flat bands in twisted materials are known to host a variety of topological phases. For instance, at filling $\nu = -3$ in twisted bilayer graphene, an interaction-induced Chern insulator has been predicted[17]. Here we focus on single-particle symmetry-breaking effects, namely tuning the strength of the electric field. For a charge-neutral system for all studied electric fields, hBN strengths and Hubbard parameters U, flat bands near the Fermi level are always intertwined. Therefore, single band Berry's curvature and Chern numbers are not well defined. However, multiband analogs can be defined, in our case of 2+2 bands separated from other bands by well-defined energy gaps, valid for an ample region in the parameter space of $\Delta_{\mathrm{hBN}}, \Delta_V$ and U. In Fig. 5a,b, we show the corresponding Hartree-Fock band structures for two representative choices of parameters (more details in SM). Details of multiband Berry's curvature calculations are shown in the "Methods" section.

First, we establish that the multiband Chern number $C_{1+2+3+4}$ corresponding to all four bands is 0. This is also the case for the two flat valence (VBs) and conduction bands (CBs) separately ($C_{1+2} = C_{3+4} = 0$). However, we observe a non-zero peak of mBC around K and K' points, see e.g., Fig 5c, which cancel each other out. We establish that non-zero peaks are also present around the Γ point, in Fig. 5c in the corners of rhomboidal moiré mBZ. In that sense, the geometry of wavefunctions is hidden since it produces $C = 0$ despite having a rich profile in the mBZ. We note that significant Berry curvature occurring at moiré K points can be intuitively understood as resulting from the Dirac cone hybridizing with the flat-bands via electric field and hBN gap. This effect provides a new scenario for the generation of topological flat-bands in trilayer moiré materials.

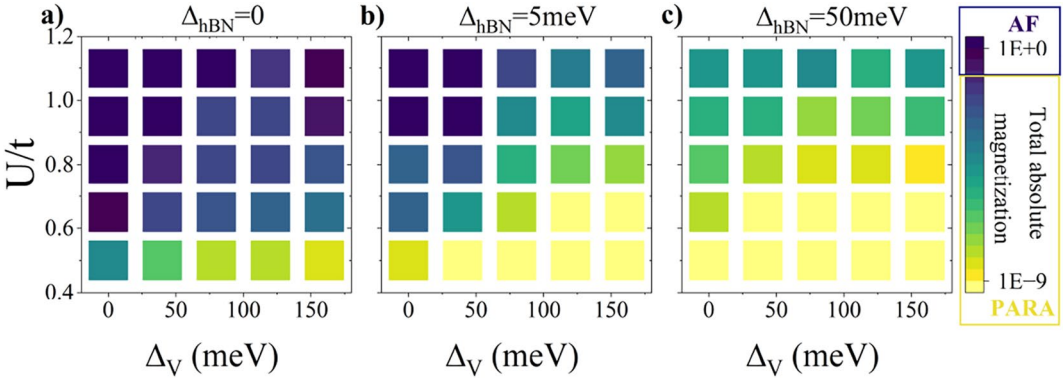

Fig. 4. Magnetic phase diagram of TTG. (**a**) TTG without a substrate. AF order parameter is studied in function of interaction strength (U/t) and applied electric potential (Δ_V) (**b**,**c**) Similar phase diagram for staggered potential strengths (**b**) $\Delta_{hBN} = 5$ meV and (**c**) $\Delta_{hBN} = 50$ meV. The color scale denotes the total absolute magnetization in logarithmic scale.

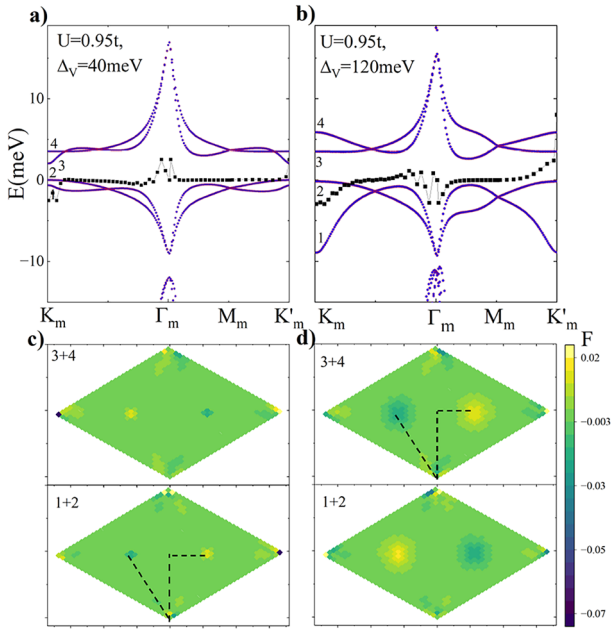

Fig. 5. Multiband Berry's curvature in TTG. Band structure and mBC profiles along the mBZ path for both two VBs (1+2) and two CBs (3+4) for (**a**) $\Delta_V = 40$ meV and (**b**) $\Delta_V = 120$ meV. Distribution of mBC on whole mBZ (**c**) corresponding to (**a**) and (**d**) corresponding to (**b**). Color scale encodes the strength of mBC. The dashed line shows the mBZ path of (**a**) and (**b**).

While a total Chern number zero implies a topologically trivial ground state for a charge-neutral system, a non-zero multiband Berry's curvature can give rise to a valley Hall effect, with the conductivity σ_{xy}^{K} determined by the integral over moiré Berry curvature over a single moiré valley. To measure such a valley current, a valley population imbalance (i.e. breaking of time-reversal symmetry) is required, for example, via circularly polarized light, as demonstrated in the experiment by Mak et al.[72] for MoS_2 monolayers. A possible mechanism for generating a moiré valley imbalance in twisted trilayer graphene is not yet known to us and will be a subject of future studies.

We also show that the k-space profiles of mBC can be tuned using an electric field. In Fig. 5c,d, we compare the distribution of BC across mBZ for two values of Δ_V, keeping fixed Δ_{hBN} and U for clarity. We observe that the spread of mBC increases for larger Δ_V around K points. A less pronounced effect is observed around the Γ point. Such curvature strength tuning, combined with the selective valley population for doped systems, might be interesting from the perspective of engineering interacting states. To verify the tunability of Berry curvature, one could employ valley-resolved transport experiment. However, such measurement necessitates creation of a moiré valley imbalance that is yet to be realized in TTG.

Discussion

Twisted trilayer graphene is a highly tunable moiré system. We predict a surprisingly small critical value of Hubbard parameter U necessary to observe magnetic phase transition between para- and anti-ferromagnetic states. This AF state is microscopic, spins are anti-aligned on neighboring graphene A and B sites inside TTG's AAA moiré centers. It is well-known that the AF state is not observed in pristine graphene because interactions are too weak. On the other hand, in TTG, this condition is weakened, although we note that such a state is destabilized by mirror and sublattice symmetry breaking perturbations. Effectively, we also expect stronger screening in our setup compared to that of suspended graphene, and further studies are necessary to establish optimal device design to reach the AF state in TTG. Such studies, including, e.g., quantum fluctuations, more realistic extended Hubbard models with long-range interaction, and better account for the dielectric environment and electron-electron screening models are the subject of our ongoing work. We note that the unrestricted collinear Hartree-Fock method used in this paper has been shown sufficient to capture the ground state properties of twisted bilayer graphene[73–76], with general qualitative picture unchanged when more precise treatments of correlations, i.e. exact diagonalization, density matrix renormalization group or dynamical mean-field theory, are used. Inclusion of correlations is the subject of our future work. We note that in the absence of the hBN substrate, we did not observe the emergence of sublattice-polarized ground states. On the other hand, the detection of spontaneously broken valley symmetry[23,26], in the context of atomistic calculation, is not as straightforward, as shown in Ref.[77].

Our findings highlight the intricate interplay of electric field, sublattice symmetry breaking, and electron-electron interactions in determining the magnetic and electronic properties of TTG. The tunability of these parameters provides a promising pathway to designing devices with controllable correlated and topological

phases. This study underscores TTG as a versatile platform to probe and manipulate quantum materials' magnetic and electronic properties.

Although topologically trivial at charge neutrality, TTG hosts nonzero peaks of multiband Berry's curvature. This curvature originates from the geometry of wave functions in the flat band and can be tuned using electric fields. This can be useful in understanding low electron/hole doped phases, especially those in which carriers unequally populate valleys, i.e., valley polarized states. It would also be interesting to establish if AF and topological phases can co-exist for realistic interactions in other multilayer systems, e.g., pentalayers with hBN-induced moiré potentials, in which fractional quantum anomalous Hall states have been recently observed[78].

During the review of this manuscript, we became aware of three recent works discussing the magnetic properties of this system. Reference[71] points out that an antiferromagnetic spin-based order is less consistent with their magnetoresistance data around $\nu = 0$, and that an orbital magnetic state is more plausible. In Ref.[37] evidence of in-plane magnetic order—contrasting with our out-of-plane order—is presented to coexisting with superconducting order around $\nu = -2$ to $\nu = -3$ hole doping. A quantum phase transition between antiferromagnetic semimetal and heavy fermion/Kondo regime is proposed in Ref.[79] near $\nu = 3$. A detailed analysis of competing magnetic states and their relative energies compared to flavor polarized or coherent states across the doping—external gate phase diagram is the subject of our future study.

Methods

Mirror-symmetric TTG is constructed by aligning the top and bottom layers and twisting the middle layer by a given angle θ. If θ belongs to a set of commensurate twist angles, moiré primitive vectors are $\vec{L}_1^{(m)} = m\vec{a}_1 - (m+1)\vec{a}_2$, $\vec{L}_2^{(m)} = -(m+1)\vec{a}_1 - (2m+1)\vec{a}_2$, where m is an integer, which is related to the twist angle θ by $\cos(\theta_m) = (3m^2 + 3m + 1/2)/(3m^2 + 3m + 1)$. Here we use $\theta = 1.55^\circ$ ($m = 21$). The number of atoms in moiré unit cell is $N_{\rm at} = 6(3m(m+1)+1)$, which here gives 8322 atoms. We account for the lattice relaxation effects along the z-axis by varying the inter-layer distance based on the stacking configuration[20,45,80]. We treat the middle layer as rigid and relax only the top and bottom layers. Relaxation leads to flattening of the flat band, renormalization of the remote bands, and gaps opening between the flat and the remote bands an the Γ point. More details of the relaxation are presented in SM.

To describe the electronic properties of TTG, we employ a tight-binding model for p_z atomic orbitals defined by Eqs. (1) and (2). We use the following parameters $a = 1.412$ Å, $c = 3.36$ Å, $\gamma_0 = -2.835$ eV, $\gamma_1 = 0.48$ eV. Here, *a* is the carbon-carbon distance, *c* is the inter-layer distance of an unrelaxed system, $\gamma_0(\gamma_1)$ is the value of the nearest in-plane (out-of-plane) neighbor hopping. The dimensionless decay constants are $\lambda_1 = 3.15$ in-plane and $\lambda_2 = 7.50$ out-of-plane. A more detailed description of the model can be found in Refs.[58,81].

The considered values of the staggered potential induced by the presence of an hBN substrate were taken to be between $0 - 50$ meV. The order of these values is consistent with experiments[59,82] and *ab initio* calculations[83–87] for different experimental set-ups, such as aligned graphene/hBN layers, entirely misaligned structure or modulated distance between TBG and the substrate.

The Hubbard repulsion term is given by $\hat{H}_U = U\sum_i \hat{n}_{i\uparrow}\hat{n}_{i\downarrow}$, where $\hat{n}_{i\sigma} = c^\dagger_{i\sigma}c_{i\sigma}$ is the spin-resolved electron number operator at site *i*. The parameter $U > 0$ is the on-site Coulomb repulsion energy. We obtain the ground state of this system in the collinear Hartree-Fock mean-field approximation, where $\hat{H}_U^{\rm MF} = U\sum_i \hat{n}_{i\uparrow}\langle\hat{n}_{i\downarrow}\rangle + \hat{n}_{i\downarrow}\langle\hat{n}_{i\uparrow}\rangle$. To study the magnetic properties of this ground state, we define the total, absolute magnetization in the units of Bohr magneton μ_B as $M = \sum_i^{N_{\rm at}} |m_{z,i}| = \sum_i^{N_{\rm at}} \frac{|\langle\hat{n}_{i\uparrow}\rangle - \langle\hat{n}_{i\downarrow}\rangle|}{2}$, where $m_{z,i}$ is the site magnetization.

We proceed numerically employing a self-consistent collinear Hartree-Fock method. We perform an all-band calculation on a 8×8 grid in the momentum space until a difference of 10^{-8} is reached between the input and output density. We use several initial guesses, some of which exploit the system's symmetry, while some are generated randomly. We note that regardless of the initial condition, we obtain qualitatively the same converged density in all cases. Depending on the interaction strength, the system needs between 50–200 iterations to converge.

Finally, we calculate the multiband Berry curvatures and Chern numbers, using a numerical procedure on a discretized Brillouin zone[88]. In the non-Abelian formulation[89], appropriate when degeneracy at band crossings is present, the Berry's connection is promoted to a matrix in band indices *m, n* given by $R_{mn} = i\langle u_{m\vec{k}}|\partial u_{n\vec{k}}/\partial\vec{k}\rangle$, where *u* are Bloch parts of electronic wavefunctions. This can further lead to Berry curvature or Wilson loop concept[90]. Here we focus on the former structure that, when traced over, gives multiband Chern number $c_\psi = (2\pi i)^{-1}\int_{BZ} tr(d\hat{R})$. To cancel out random numerical phases in Bloch wavefunctions, we follow[88] and define *n*-bands link variable $U_\mu(\vec{k}_i)$ from the chosen set of wavefunctions $\psi = (|\phi_1\rangle, ..., |\phi_n\rangle)$ as $U_\mu(\vec{k}_i) \equiv \det\psi^\dagger(\vec{k}_i)\psi(\vec{k}_i + \hat{\mu})/|\det\psi^\dagger(\vec{k}_i)\psi(\vec{k}_i + \hat{\mu})|$. Here, $\mu = 1, 2$ represents the possible directions in 2D while $\hat{\mu}$ is the vector connecting the nearest *i*-th *k* point to its nearest neighbor in direction μ. From the link variable, we can define mBC as $F(\vec{k}_i) = \ln\left(U_1(\vec{k}_i)U_2(\vec{k}_i + \hat{1})U_1(\vec{k}_i + \hat{2})^{-1}U_2(\vec{k}_i)^{-1}\right)$. The Chern number for the *n* bands is then defined $c_\psi \equiv (2\pi i)^{-1}\sum_i F(\vec{k}_i)$. Note that since $U_\mu(\vec{k}_i)$ is normalized, $F(\vec{k}_i)$ is purely imaginary, and the Chern number c_ψ is real. Since non-Abelian curvature enters equation of motion for the wave packet in the same manner as Abelian one, the anomalous velocity related to non-zero *R* gives rise to anomalous Hall response.

Data availability

The data that support the findings of this study are available from the corresponding author upon reasonable request.

Received: 24 November 2025; Accepted: 30 March 2026
Published online: 18 April 2026

References

1. Cao, Y. et al. Correlated insulator behaviour at half-filling in magic-angle graphene superlattices. *Nature* **556**, 80. https://doi.org/10.1038/nature26154 (2018).
2. Cao, Y. et al. Unconventional superconductivity in magic-angle graphene superlattices. *Nature* **556**, 43. https://doi.org/10.1038/nature26160 (2018).
3. Bistritzer, R. & MacDonald, A. H. Moiré bands in twisted double-layer graphene. *Proc. Natl. Acad. Sci.* **108**, 12233. https://doi.org/10.1073/pnas.1108174108 (2011).
4. Park, J. M., Cao, Y., Watanabe, K., Taniguchi, T. & Jarillo-Herrero, P. Tunable strongly coupled superconductivity in magic-angle twisted trilayer graphene. *Nature* **590**, 249. https://doi.org/10.1038/s41586-021-03192-0 (2021).
5. Hao, Z. et al. Electric field-tunable superconductivity in alternating-twist magic-angle trilayer graphene. *Science* **371**, 1133. https://doi.org/10.1126/science.abg0399 (2021).
6. Cao, Y., Park, J. M., Watanabe, K., Taniguchi, T. & Jarillo-Herrero, P. Pauli-limit violation and re-entrant superconductivity in moiré graphene. *Nature* **595**, 526. https://doi.org/10.1038/s41586-021-03685-y (2021).
7. Devakul, T. et al. Magic-angle helical trilayer graphene. *Sci. Adv.* **9**, eadi6063. https://doi.org/10.1126/sciadv.adi6063 (2023).
8. Su, R., Kuiri, M., Watanabe, K., Taniguchi, T. & Folk, J. Superconductivity in twisted double bilayer graphene stabilized by WSe_2. *Nat. Mater.* **22**, 1332. https://doi.org/10.1038/s41563-023-01653-7 (2023).
9. Han, T. et al. Correlated insulator and Chern insulators in pentalayer rhombohedral-stacked graphene. *Nat. Nanotechnol.* **19**, 181. https://doi.org/10.1038/s41565-023-01520-1 (2024).
10. Tang, Y. et al. Simulation of Hubbard model physics in WSe_2/WS_2 moiré superlattices. *Nature* **579**, 353. https://doi.org/10.1038/s41586-020-2085-3 (2020).
11. Shen, C. et al. Correlated states in twisted double bilayer graphene. *Nat. Phys.* **16**, 520. https://doi.org/10.1038/s41567-020-0825-9 (2020).
12. Cao, Y. et al. Tunable correlated states and spin-polarized phases in twisted bilayer-bilayer graphene. *Nature* **583**, 215. https://doi.org/10.1038/s41586-020-2260-6 (2020).
13. Liu, X. et al. Tunable spin-polarized correlated states in twisted double bilayer graphene. *Nature* **583**, 221. https://doi.org/10.1038/s41586-020-2458-7 (2020).
14. Chen, S. et al. Electrically tunable correlated and topological states in twisted monolayer–bilayer graphene. *Nat. Phys.* **17**, 374. https://doi.org/10.1038/s41567-020-01062-6 (2021).
15. Chen, G. et al. Evidence of a gate-tunable Mott insulator in a trilayer graphene moiré superlattice. *Nat. Phys.* **15**, 237. https://doi.org/10.1038/s41567-018-0387-2 (2019).
16. Serlin, M. et al. Intrinsic quantized anomalous Hall effect in a moiré heterostructure. *Science* **367**, 900. https://doi.org/10.1126/science.aay5533 (2020).
17. Sharpe, A. L. et al. Emergent ferromagnetism near three-quarters filling in twisted bilayer graphene. *Science* **365**, 605. https://doi.org/10.1126/science.aaw3780 (2019).
18. Regan, E. C. et al. Mott and generalized Wigner crystal states in WSe_2/WS_2 moiré superlattices. *Nature* **579**, 359. https://doi.org/10.1038/s41586-020-2092-4 (2020).
19. Khalaf, E., Kruchkov, A. J., Tarnopolsky, G. & Vishwanath, A. Magic angle hierarchy in twisted graphene multilayers. *Phys. Rev. B* **100**, 085109. https://doi.org/10.1103/PhysRevB.100.085109 (2019).
20. Carr, S. et al. Ultraheavy and ultrarelativistic Dirac quasiparticles in sandwiched graphenes. *Nano Lett.* **20**, 3030. https://doi.org/10.1021/acs.nanolett.9b04979 (2020).
21. Călugăru, D. et al. Twisted symmetric trilayer graphene: single-particle and many-body Hamiltonians and hidden nonlocal symmetries of trilayer moiré systems with and without displacement field. *Phys. Rev. B* **103**, 195411. https://doi.org/10.1103/PhysRevB.103.195411 (2021).
22. Lei, C., Linhart, L., Qin, W., Libisch, F. & MacDonald, A. H. Mirror symmetry breaking and lateral stacking shifts in twisted trilayer graphene. *Phys. Rev. B* **104**, 035139. https://doi.org/10.1103/PhysRevB.104.035139 (2021).
23. Xie, F., Regnault, N., Călugăru, D., Bernevig, B. A. & Lian, B. Twisted symmetric trilayer graphene. II. Projected Hartree-Fock study. *Phys. Rev. B* **104**, 115167. https://doi.org/10.1103/PhysRevB.104.115167 (2021).
24. Phong, V. O. T., Pantaleón, P. A., Cea, T. & Guinea, F. Band structure and superconductivity in twisted trilayer graphene. *Phys. Rev. B* **104**, L121116. https://doi.org/10.1103/PhysRevB.104.L121116 (2021).
25. Ledwith, P.J., Khalaf, E., Zhu, Z., Carr, S., Kaxiras, E. & Vishwanath, A. TB or not TB? Contrasting properties of twisted bilayer graphene and the alternating twist n-layer structures ($n = 3, 4, 5, \ldots$). arXiv arXiv: 2111.11060 [cond-mat.str-el] (2021).
26. Christos, M., Sachdev, S. & Scheurer, M. S. Correlated insulators, semimetals, and superconductivity in twisted trilayer graphene. *Phys. Rev. X* **12**, 021018. https://doi.org/10.1103/PhysRevX.12.021018 (2022).
27. Yu, J., Xie, M., Bernevig, B. A. & Das Sarma, S. Magic-angle twisted symmetric trilayer graphene as a topological heavy-fermion problem. *Phys. Rev. B* **108**, 035129. https://doi.org/10.1103/PhysRevB.108.035129 (2023).
28. Li, Y. et al. Observation of coexisting Dirac bands and moiré flat bands in magic-angle twisted trilayer graphene. *Adv. Mater.* **34**, 2205996. https://doi.org/10.1002/adma.202205996 (2022).
29. Zhang, Y. et al. Promotion of superconductivity in magic-angle graphene multilayers. *Science* **377**, 1538. https://doi.org/10.1126/science.abn8585 (2022).
30. Kim, H. et al. Evidence for unconventional superconductivity in twisted trilayer graphene. *Nature* **606**, 494. https://doi.org/10.1038/s41586-022-04715-z (2022).
31. Lin, J.-X. et al. Zero-field superconducting diode effect in small-twist-angle trilayer graphene. *Nat. Phys.* **18**, 1221. https://doi.org/10.1038/s41567-022-01700-1 (2022).
32. Liu, X., Zhang, N. J., Watanabe, K., Taniguchi, T. & Li, J. I. A. Isospin order in superconducting magic-angle twisted trilayer graphene. *Nat. Phys.* **18**, 522. https://doi.org/10.1038/s41567-022-01515-0 (2022).
33. Park, J. M. et al. Robust superconductivity in magic-angle multilayer graphene family. *Nat. Mater.* **21**, 877. https://doi.org/10.1038/s41563-022-01287-1 (2022).
34. Siriviboon, P., Lin, J.-X., Liu, X., Scammell, H.D., Liu, S., Rhodes, D., Watanabe, K., Taniguchi, T., Hone, J., Scheurer, M. S. & Li, J. I. A. A new flavor of correlation and superconductivity in small twist-angle trilayer graphene. arXiv arXiv: 2112.07127 [cond-mat.mes-hall] (2022).
35. Kim, H. et al. Imaging inter-valley coherent order in magic-angle twisted trilayer graphene. *Nature* **623**, 942. https://doi.org/10.1038/s41586-023-06663-8 (2023).

36. Shen, C. et al. Dirac spectroscopy of strongly correlated phases in twisted trilayer graphene. *Nat. Mater.* **22**, 316. https://doi.org/10.1038/s41563-022-01428-6 (2023).
37. Mukherjee, A. et al. Superconducting magic-angle twisted trilayer graphene with competing magnetic order and moiré inhomogeneities. *Nat. Mater.* **24**, 1400. https://doi.org/10.1038/s41563-025-02252-4 (2025).
38. Batlle-Porro, S., Calugaru, D., Hu, H., Kumar, R. K., Hesp, N. C. H., Watanabe, K., Taniguchi, T., Bernevig, B. A., Stepanov, P. & Koppens, F. H. L. Cryo-near-field photovoltage microscopy of heavy-fermion twisted symmetric trilayer graphene. arXiv arXiv: 2402.12296 [cond-mat.mes-hall] (2024).
39. Zhang, N. J. et al. Angle-resolved transport non-reciprocity and spontaneous symmetry breaking in twisted trilayer graphene. *Nat. Mater.* **23**, 356. https://doi.org/10.1038/s41563-024-01809-z (2024).
40. Zhou, Z., Jiang, J., Karnatak, P., Wang, Z., Wagner, G., Watanabe, K., Taniguchi, T., Schönenberger, C., Parameswaran, S. A., Simon, S. H. & Banerjee, M. Double-dome unconventional superconductivity in twisted trilayer graphene. arXiv arXiv: 2404.09909 [cond-mat.mes-hall] (2024).
41. Banerjee, A. et al. Superfluid stiffness of twisted trilayer graphene superconductors. *Nature* **638**, 93 (2025).
42. Pierce, A. T. et al. Tunable interplay between light and heavy electrons in twisted trilayer graphene. *Nat. Phys.* **21**, 1237. https://doi.org/10.1038/s41567-025-02956-z (2025).
43. Park, J. M., Sun, S., Watanabe, K., Taniguchi, T. & Jarillo-Herrero, P. Experimental evidence for nodal superconducting gap in moiré graphene. *Science* **391**, 79. https://doi.org/10.1126/science.adv8376 (2026).
44. Kim, H. et al. Resolving intervalley gaps and many-body resonances in moiré superconductors. *Nature* **650**, 592. https://doi.org/10.1038/s41586-025-10067-1 (2026).
45. Fischer, A. et al. Unconventional superconductivity in magic-angle twisted trilayer graphene. *npj Quantum Mater.* **7**, 5. https://doi.org/10.1038/s41535-021-00410-w (2022).
46. Qin, W. & MacDonald, A. H. In-plane critical magnetic fields in magic-angle twisted trilayer graphene. *Phys. Rev. Lett.* **127**, 097001. https://doi.org/10.1103/PhysRevLett.127.097001 (2021).
47. Chou, Y.-Z., Wu, F., Sau, J. D. & Das Sarma, S. Correlation-induced triplet pairing superconductivity in graphene-based moiré systems. *Phys. Rev. Lett.* **127**, 217001. https://doi.org/10.1103/PhysRevLett.127.217001 (2021).
48. Lake, E. & Senthil, T. Reentrant superconductivity through a quantum Lifshitz transition in twisted trilayer graphene. *Phys. Rev. B* **104**, 174505. https://doi.org/10.1103/PhysRevB.104.174505 (2021).
49. González, J. & Stauber, T. Ising superconductivity induced from spin-selective valley symmetry breaking in twisted trilayer graphene. *Nat. Commun.* **14**, 2746. https://doi.org/10.1038/s41467-023-38250-w (2023).
50. Samajdar, R., Teng, Y. & Scheurer, M. S. Moiré phonons and impact of electronic symmetry breaking in twisted trilayer graphene. *Phys. Rev. B* **106**, L201403. https://doi.org/10.1103/PhysRevB.106.L201403 (2022).
51. Sorella, S. & Tosatti, E. Semi-metal-insulator transition of the Hubbard model in the honeycomb lattice. *Europhys. Lett.* **19**, 699. https://doi.org/10.1209/0295-5075/19/8/007 (1992).
52. Yazyev, O. V. Emergence of magnetism in graphene materials and nanostructures. *Rep. Prog. Phys.* **73**, 056501. https://doi.org/10.1088/0034-4885/73/5/056501 (2010).
53. Güçlü, A. D., Potasz, P., Korkusinski, M. & Hawrylak, P. Magnetic properties of gated graphene nanostructures. In *Graphene Quantum Dots* 111–144 (Springer, 2014). https://doi.org/10.1007/978-3-662-44611-9_6
54. Vahedi, J., Peters, R., Missaoui, A., Honecker, A. & de Laissardiere, G. T. Magnetism of magic-angle twisted bilayer graphene. *SciPost Phys.* **11**, 083. https://doi.org/10.21468/SciPostPhys.11.4.083 (2021).
55. Jiang, K., Zhou, S., Dai, X. & Wang, Z. Antiferromagnetic Chern insulators in noncentrosymmetric systems. *Phys. Rev. Lett.* **120**, 157205. https://doi.org/10.1103/PhysRevLett.120.157205 (2018).
56. Yu, J. et al. Quantum geometry in quantum materials. *Npj Quantum Materials* **10**, 101. https://doi.org/10.1038/s41535-025-00801-3 (2025).
57. Zhang, Z., Yang, J., Xie, B., Feng, Z., Zhang, S., Watanabe, K., Taniguchi, T., Yang, X., Dai, Q., Liu, T., Liu, D., Liu, K., Song, Z., Liu, J. & Lu, X. Commensurate and incommensurate Chern insulators in magic-angle bilayer graphene. arXiv arXiv: 2408.12509 [cond-mat.mes-hall] (2024).
58. Wania Rodrigues, A. et al. Atomistic theory of the moiré Hofstadter butterfly in magic-angle graphene. *Phys. Rev. B* **109**, 075166. https://doi.org/10.1103/PhysRevB.109.075166 (2024).
59. Hunt, B. et al. Massive Dirac Fermions and Hofstadter Butterfly in a van der Waals heterostructure. *Science* **340**, 1427. https://doi.org/10.1126/science.1237240 (2013).
60. Vidarte, K. J. U., Riffo, F. P., Morell, E. S. & Lewenkopf, C. Stoner ferromagnetism in low-angle twisted bilayer graphene at three-quarters filling. *Phys. Rev. B* **111**, 045164. https://doi.org/10.1103/PhysRevB.111.045164 (2025).
61. Hou, R., Sur, S., Wagner, L. K. & Nevidomskyy, A. H. Particle-hole asymmetric phases in doped twisted bilayer graphene. *Phys. Rev. B* **111**, 125140. https://doi.org/10.1103/PhysRevB.111.125140 (2025).
62. Sánchez Sánchez, M., González, J. & Stauber, T. Nonflat bands and chiral symmetry in magic-angle twisted bilayer graphene. *Phys. Rev. B* **111**, 205133. https://doi.org/10.1103/PhysRevB.111.205133 (2025).
63. Adhikari, K., Seo, K., Beach, K. S. D. & Uchoa, B. Strongly interacting phases in twisted bilayer graphene at the magic angle. *Phys. Rev. B* **110**, L121123. https://doi.org/10.1103/PhysRevB.110.L121123 (2024).
64. Ryu, H. et al. Temperature-dependent electron-electron interaction in graphene on SrTiO3. *Nano Lett.* **17**, 5914. https://doi.org/10.1021/acs.nanolett.7b01650 (2017).
65. Goodwin, Z. A. H. et al. Critical role of device geometry for the phase diagram of twisted bilayer graphene. *Phys. Rev. B* **101**, 165110. https://doi.org/10.1103/PhysRevB.101.165110 (2020).
66. Goodwin, Z. A. H., Corsetti, F., Mostofi, A. A. & Lischner, J. Attractive electron-electron interactions from internal screening in magic-angle twisted bilayer graphene. *Phys. Rev. B* **100**, 235424. https://doi.org/10.1103/PhysRevB.100.235424 (2019).
67. Hou, Y. et al. Strain engineering of twisted bilayer graphene: The rise of strain-Twistronics. *Small* **21**, 2311185. https://doi.org/10.1002/smll.202311185 (2025).
68. Nuckolls, K. P. & Yazdani, A. A microscopic perspective on moiré materials. *Nat. Rev. Mater.* **9**, 460. https://doi.org/10.1038/s41578-024-00682-1 (2024).
69. Tang, Y. et al. Simulation of Hubbard model physics in WSE2/WS2 moiré superlattices. *Nature* **579**, 353. https://doi.org/10.1038/s41586-020-2085-3 (2020).
70. Cheon, C.-Y. et al. Nature of 2D XY antiferromagnetism in a van der Waals monolayer. *Nat. Commun.* **17**, 60. https://doi.org/10.1038/s41467-025-66672-1 (2025).
71. Bhardwaj, V. et al. Gate-tunable orbital magnetism and competing superconductivity in twisted trilayer graphene Josephson junctions. *ACS Appl. Mater. Interfaces* **17**, 69784. https://doi.org/10.1021/acsami.5c15822 (2025).
72. Mak, K. F., McGill, K. L., Park, J., & McEuen, P. L. The valley Hall effect in MoS2 transistors. Science, **344**,1489–1492. https://doi.org/10.1126/science.1250140 (2014).
73. Soejima, T., Parker, D. E., Bultinck, N., Hauschild, J. & Zaletel, M. P. Efficient simulation of moiré materials using the density matrix renormalization group. *Phys. Rev. B* **102**, 205111. https://doi.org/10.1103/PhysRevB.102.205111 (2020).
74. Potasz, P., Xie, M. & MacDonald, A. H. Exact diagonalization for magic-angle twisted bilayer graphene. *Phys. Rev. Lett.* **127**, 147203. https://doi.org/10.1103/PhysRevLett.127.147203 (2021).
75. Xie, F. et al. Twisted bilayer graphene. VI. An exact diagonalization study at nonzero integer filling. *Phys. Rev. B* **103**, 205416. https://doi.org/10.1103/PhysRevB.103.205416 (2021).

76. Rai, G. et al. Dynamical correlations and order in magic-angle twisted bilayer graphene. *Phys. Rev. X* **14**, 031045. https://doi.org/10.1103/PhysRevX.14.031045 (2024).
77. Sánchez Sánchez, M., Díaz, I., González, J. & Stauber, T. Nematic versus Kekulé phases in twisted bilayer graphene under hydrostatic pressure. *Phys. Rev. Lett.* **133**, 266603. https://doi.org/10.1103/PhysRevLett.133.266603 (2024).
78. Lu, Z. et al. Fractional quantum anomalous Hall effect in multilayer graphene. *Nature* **626**, 759. https://doi.org/10.1038/s41586-023-07010-7 (2024).
79. Zhang, L., Zhou, W., Fang, X., Zhan, Z., Watanabe, K., Taniguchi, T., feng Yang, Y. & Xu, S. Electrically tunable heavy fermion and quantum criticality in magic-angle twisted trilayer graphene. arXiv arXiv: 2507.12254 [cond-mat.mes-hall] (2025).
80. Lopez-Bezanilla, A. & Lado, J. L. Electrical band flattening, valley flux, and superconductivity in twisted trilayer graphene. *Phys. Rev. Res.* **2**, 033357. https://doi.org/10.1103/PhysRevResearch.2.033357 (2020).
81. Trambly de Laissardière, G., Mayou, D. & Magaud, L. Localization of Dirac electrons in rotated graphene bilayers. *Nano Lett.* **10**, 804. https://doi.org/10.1021/nl902948m (2010).
82. Woods, C. R. et al. Commensurate–incommensurate transition in graphene on hexagonal boron nitride. *Nat. Phys.* **10**, 451. https://doi.org/10.1038/nphys2954 (2014).
83. Giovannetti, G., Khomyakov, P. A., Brocks, G., Kelly, P. J. & van den Brink, J. Substrate-induced band gap in graphene on hexagonal boron nitride: Ab initio density functional calculations. *Phys. Rev. B* **76**, 073103. https://doi.org/10.1103/PhysRevB.76.073103 (2007).
84. Sławińska, J., Zasada, I. & Klusek, Z. Energy gap tuning in graphene on hexagonal boron nitride bilayer system. *Phys. Rev. B* **81**, 155433. https://doi.org/10.1103/PhysRevB.81.155433 (2010).
85. Sachs, B., Wehling, T. O., Katsnelson, M. I. & Lichtenstein, A. I. Adhesion and electronic structure of graphene on hexagonal boron nitride substrates. *Phys. Rev. B* **84**, 195414. https://doi.org/10.1103/PhysRevB.84.195414 (2011).
86. Zollner, K., Gmitra, M. & Fabian, J. Heterostructures of graphene and hBN: electronic, spin-orbit, and spin relaxation properties from first principles. *Phys. Rev. B* **99**, 125151. https://doi.org/10.1103/PhysRevB.99.125151 (2019).
87. Zollner, K., Cummings, A. W., Roche, S. & Fabian, J. Graphene on two-dimensional hexagonal BN, ALN, and GAN: electronic, spin-orbit, and spin relaxation properties. *Phys. Rev. B* **103**, 075129. https://doi.org/10.1103/PhysRevB.103.075129 (2021).
88. Fukui, T., Hatsugai, Y. & Suzuki, H. Chern numbers in discretized Brillouin zone: Efficient method of computing (spin) Hall conductances. *J. Phys. Soc. Jpn.* **74**, 1674–1677. https://doi.org/10.1143/jpsj.74.1674 (2005).
89. Xiao, D., Chang, M.-C. & Niu, Q. Berry phase effects on electronic properties. *Rev. Mod. Phys.* **82**, 1959. https://doi.org/10.1103/RevModPhys.82.1959 (2010).
90. Yu, R., Qi, X. L., Bernevig, A., Fang, Z. & Dai, X. Equivalent expression of F_2 topological invariant for band insulators using the non-abelian berry connection. *Phys. Rev. B* **84**, 075119. https://doi.org/10.1103/PhysRevB.84.075119 (2011).
91. Digital Research Alliance of Canada. Digital Research Alliance of Canada. Howpublished. www.alliancecan.ca.

Acknowledgements

This paper was partly enabled by support provided by the Digital Research Alliance of Canada[91].

Author contributions

A.W.R., M.B. and D.M. performed the numerical calculations. A.W.R., M.B., D.M. and P.H. performed data analysis, discussed the results and wrote the manuscript with input from all co-authors.

Funding

A.W.R., D.M. and P.H. were supported by NSERC Discovery Grant No. RGPIN 2019-05714, NSERC Alliance Quantum Grant No. ALLRP/578466-2022, the QSP-078 project of the Quantum Sensors Program at the National Research Council of Canada, University of Ottawa Research Chair in Quantum Theory of Materials, Nanostructures, and Devices. M.B. has been supported by the National Science Centre, Poland, under Grant No. 2021/43/D/ST3/01989.

Declarations

Competing interests

The authors declare no competing interests.

Additional information

Supplementary Information The online version contains supplementary material available at https://doi.org/10.1038/s41598-026-47245-8.

Correspondence and requests for materials should be addressed to A.W.R.